scientific reports

Check for updates

OPEN

Photoluminescence study of optical transitions in spinel zinc gallium oxide thin films

Chengyun Shou[1], Tianchen Yang[1], Kaden Ren[1,2], Abdullah Almujtabi[1], Edward Zhu[1], Quazi Sanjid Mahmud[1], Yuan Li[1] & Jianlin Liu[1]✉

Spinel $ZnGa_2O_4$ is an ultra-wide bandgap material that can have a great potential for deep ultraviolet (UV) photonics and other applications. In this work, zinc gallium oxide (ZnGaO) samples with Zn composition ranging from 0.0 to 48.0 at% were grown in a plasma-assisted molecular beam epitaxy system. The change of crystal structure from beta to spinel was determined using reciprocal space mapping in x-ray diffraction. When Zn composition is at 0.0, 0.9, 3.4, and above 7.3 at%, the crystal structure exhibits beta phase, mixture phase, weak spinel phase, and strong spinel phase, respectively. Comprehensive photoluminescence (PL) of the samples were carried out using an ArF laser excitation, and PL peak deconvolution was performed to understand the optical transitions and energy levels within the forbidden gap. For spinel ZnGaO samples, five deconvoluted peaks were observed, revealing the energy levels of three oxygen vacancies, self-trapped holes binding energy, and acceptor levels.

Keywords Photoluminescence, Spinel zinc gallium oxide, Ultra-wide bandgap semiconductors, Phase transition, Self-trapped holes

Gallium oxide (Ga_2O_3), one of the ultra-wide bandgap (UWBG) semiconductors with a bandgap of ~ 4.9 eV, attracted much attention in the past several years due to its promising applications in power electronics and deep ultraviolet (UV) photonics[1–6]. Ga_2O_3 has five polymorphous: α-phase (rhombohedral), β-phase (monoclinic), γ-phase (spinel), δ-phase (body-centered cubic), and ε-phase (hexagonal)[7]. Among these polymorphous, β-phase is the most stable. β-phase Ga_2O_3 is a direct bandgap semiconductor and has high critical electric field strength and high Baliga's figures of merit[8–10]. Despite extensive studies of Ga_2O_3, many challenges are still not resolved[11–14]. One of them is to find a suitable p-type dopant that can enhance its potential for practical applications such as deep-UV lasers. When the composition of a p-type dopant is tuned in a wide range, not only electrical and optical properties but also crystal structure will change. For example, excessive incorporation of Mg into Ga_2O_3 increases the bandgaps of the resultant materials within a range of 4.9 eV and 7.8 eV[15], and induces a phase transition from beta to rocksalt phases[16].

On the other hand, incorporation of elements such as zinc into Ga_2O_3 can decrease the bandgap. The bandgap is expected to be tuned within the range of approximately 4.9 eV and 3.3 eV by tuning the Zn composition in zinc gallium oxide (ZnGaO) alloy[17–19]. Meanwhile, the crystal structure is expected to change from beta to spinel, and to Wurtzite[20]. Many studies showed that Ga-doped Wurtzite phase ZnO is an excellent transparent conducting oxide and Zn-doped β-phase Ga_2O_3 has great potential in solar-blind photodetectors[18,19,21–24]. However, spinel structure $ZnGa_2O_4$ having a bandgap of approximately 5.2 eV has not yet been fully studied[25–27]. These materials can be used in deep-UV optoelectronic and high-power electronic applications[26,28,29]. To fully realize the potential of spinel $ZnGa_2O_4$ for various electronic and optoelectronic applications, we must understand its band structure. In the recent years, researchers used photoluminescence (PL) to understand the optical transitions of spinel ZnGaO[30–35] and doped samples using Ni[36], Bi[37], Cr[38–40], Mn[41–45], and other dopants[46–48]. Nevertheless, these prior PL studies had used lasers with excitation energies less than the bandgap energy of these materials, leading to impossible pumping of electrons from valence band to conduction band. In addition, self-trapped holes (STHs) are assumed to exist in Ga_2O_3 and ZnGaO materials[49–51]. Although their binding to certain defects or atoms was predicted by density functional theory[51], experimental validation of their binding energies has not been carried out. In this work, ZnGaO samples were grown using plasma-assisted molecular beam epitaxy (MBE). While chemical vapor deposition (CVD), pulsed laser deposition (PLD) and other tools are widely used, MBE is known to also produce high-quality oxide semiconductors including β-Ga_2O_3[52–55], ZnO[56–58], etc. Here, the effect of different Zn compositions on the crystal structure and optical property of ZnGaO thin films was

[1]Department of Electrical and Computer Engineering, University of California, Riverside, CA 92521, USA. [2]Martin Luther King High School, Riverside, CA 92508, USA. ✉email: jianlin@ece.ucr.edu

Sample #	Thickness (nm)	EDX Ga (at%)	EDX Zn (at%)	XPS Ga (at%)	XPS Zn (at%)	XPS O (at%)	Bandgap (eV)	Structure	Lattice parameters (Å) [theta/2theta] (in-plane RSM)
1	325 ± 4	100.0	0.0	27.2	0.0	72.8	4.96	Beta phase	[a = 12.09] (b = 3.02) [c = 5.75]
2	382 ± 3	99.1	0.9	26.6	0.1	73.2	5.02	Mixture phase	(a = b = c = 8.27)
3	424 ± 3	96.6	3.4	28.1	0.2	71.7	5.01	Spinel phase	(a = b = c = 8.25)
4	286 ± 4	92.7	7.3	27.6	0.7	71.7	5.04		(a = b = c = 8.29)
5	279 ± 4	83.5	16.5	25.3	3.2	71.5	5.10		(a = b = c = 8.34)
6	345 ± 3	66.9	33.1	20.6	8.9	70.5	5.02		(a = b = c = 8.34)
7	417 ± 2	56.1	43.9	15.5	12.2	72.3	4.92		(a = b = c = 8.34)
8	418 ± 2	54.8	45.2	15.8	13.0	71.3	4.89		(a = b = c = 8.34)
9	314 ± 6	52.0	48.0	14.0	13.9	72.1	4.84		(a = b = c = 8.35)

Table 1. Film thickness, Ga, Zn, and O atomic composition, optical bandgap, crystal structure and lattice parameters of ZnGaO samples.

studied. In particular, PL studies using a 193 nm ArF laser with an excitation energy of 6.42 eV were performed on the ZnGaO thin films to understand their optical transition energy levels within the forbidden gap and STH binding energies.

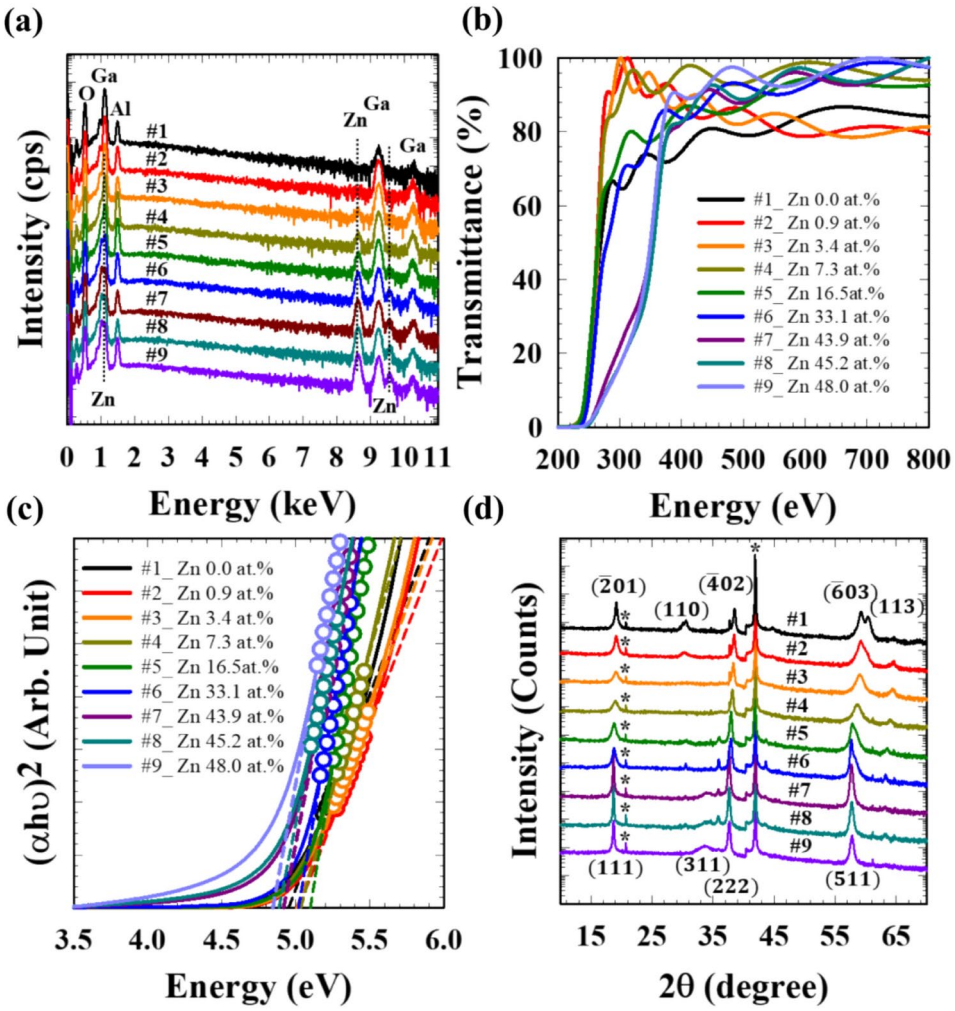

Fig. 1. (**a**) EDX spectra of all ZnGaO samples. (**b**) Transmittance spectra of all ZnGaO samples. (**c**) Tauc plot absorption spectra of all ZnGaO samples. (**d**) XRD pattern in θ/2θ scan mode of all ZnGaO samples.

Results and discussion

Table 1 shows the structural and compositional results of nine ZnGaO samples with Zn composition ranging from 0 to 48.0 at% and film thickness ranging from ~ 280 to ~ 420 nm. Figure 1a shows EDX spectra of all samples. The peaks located at 0.53, 1.01, 1.10, and 1.49 keV correspond to oxygen, zinc, gallium, and aluminum, respectively, and a signal at 0.27 keV is due to adventitious carbon. Here, only the composition ratio between Ga and Zn has been estimated, as shown in Table 1, while oxygen atomic percentage is not included because the O peaks in EDX spectra include contributions from both the film and substrate as a result of large electron beam penetration depth. The EDX 1.01 keV peak intensity increases as Zn composition increases from sample 1–9. SEM images of all samples with different compositions are shown in Fig. S1 in the supporting material. Figure S2 shows XPS survey spectra of all samples. The peaks with binding energies located at ~ 1118.1, ~ 1145.0, ~ 1022.0, ~ 1045.2, and ~ 530.9 eV correspond to Ga $2p_{3/2}$, Ga $2p_{1/2}$, Zn $2p_{3/2}$, Zn $2p_{1/2}$, and O 1s, respectively. The peak areas of Zn, Ga, and O were extracted to calculate the atomic percentage of each element for each sample, which is listed in Table 1. The Fermi level locations were also extracted from XPS valence band spectra, which are shown in Fig. S3. All samples show n-type characteristics since the Fermi levels are located in the upper portion of the forbidden gap.

Figure 1b shows transmittance spectra of ZnGaO samples by using the equation: $A = 2 - log(\%T)$, where A is the absorbance and T is the transmittance. All samples show high transmittance in the visible spectral range. Figure 1c shows Tauc plot absorption spectra of all ZnGaO samples. Absorbance spectra were obtained and converted into absorption coefficient using the equation $\alpha = 2.303 \times \frac{A}{t}$, where α is the absorption coefficient, A is absorbance obtained from the spectrometer, and t is the film thickness in centimeters. Optical bandgap can be extracted by linear extrapolation of Tauc plot onto the x-axis using the equation $(\alpha h\upsilon)^2 = c(h\nu - Eg)$, where h is Planck's constant, ν is frequency, c is constant, and E_g is optical bandgap. Figure S4 shows a plot of

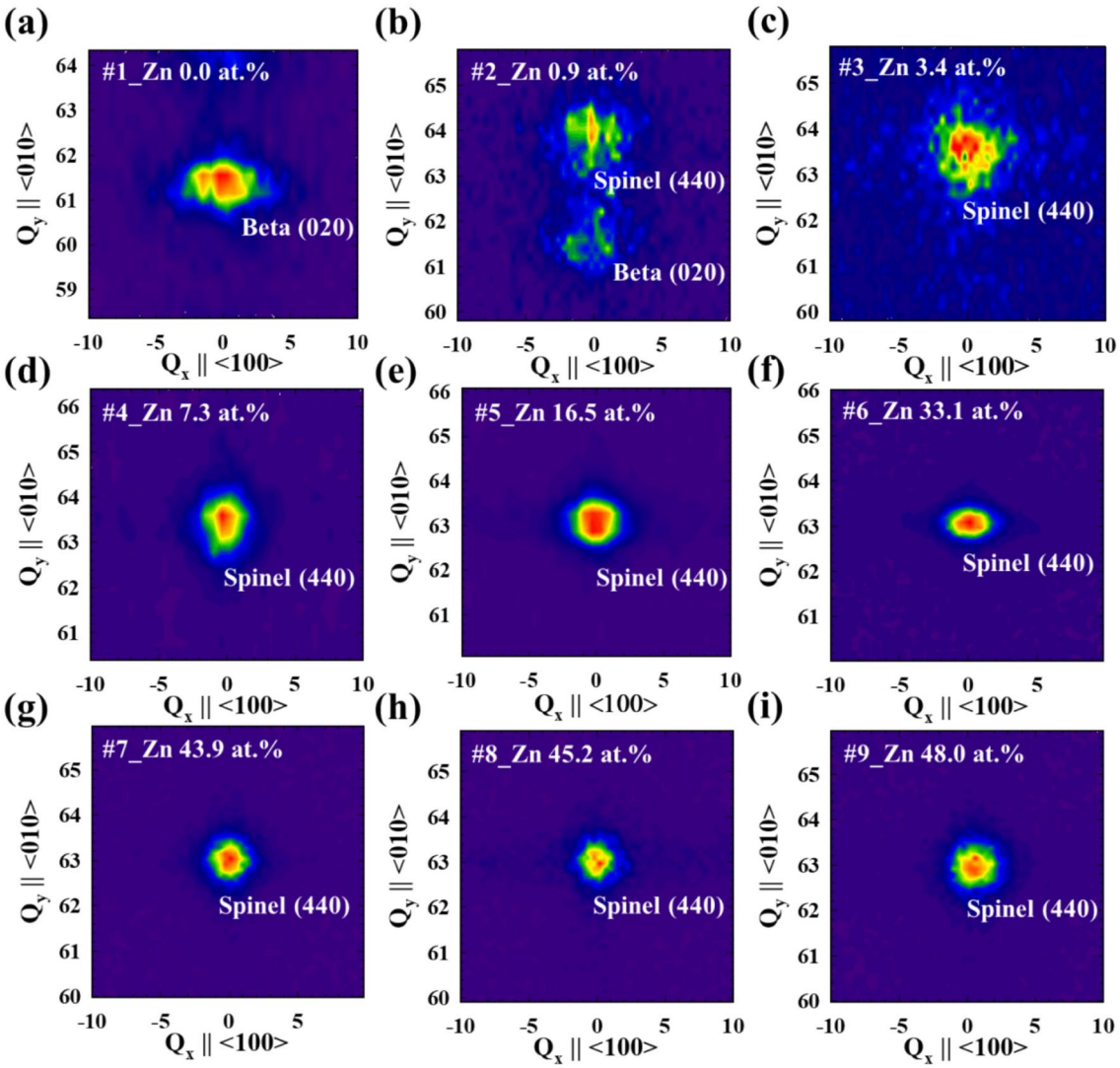

Fig. 2. XRD in-plane RSM of (**a**) beta structure (020) plane for sample 1, (**b**) mixture of beta structure (020) plane and spinel structure (440) plane for sample 2, (**c**) weak spinel structure (440) plane for sample 3, and (**d**)-(**f**) strong spinel structure (440) plane for sample 4–9.

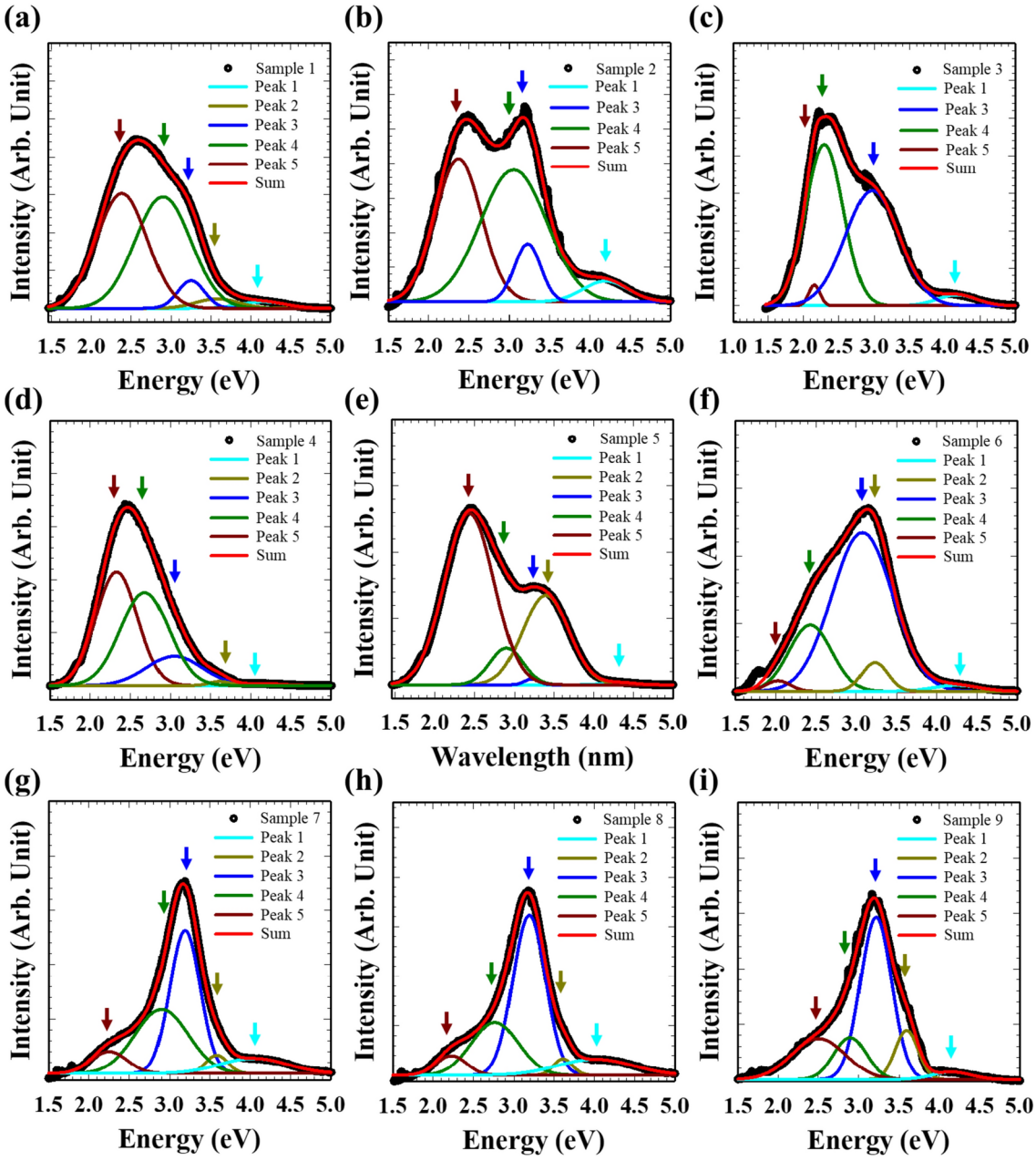

Fig. 3. Room temperature photoluminescence spectra under 193 nm laser excitation and their peak deconvolutions of ZnGaO samples with Zn composition of (**a**) 0.0 at%, (**b**) 0.9 at%, (**c**) 3.4 at%, (**d**) 7.3 at%, (**e**) 16.5 at%, (**f**) 33.1 at%, (**g**) 43.9 at%, (**h**) 45.2 at%, and (**i**) 48.0 at%.

bandgap versus Zn composition. The optical bandgaps of sample 1–5 seem to increase although undulate slightly around 5 eV or so as Zn composition increases, which may be due to the change of crystal structure from beta phase to spinel phase as seen in XRD studies later. The bandgap monotonously decreases from ~ 5 to 4.84 eV as Zn continues to increase in pure spinel phase sample 5 to sample 9.

Figure 1d shows XRD $\theta/2\theta$ scan pattern of ZnGaO samples. Peaks located at ~ 20.6° and ~ 61.1° are background signal, which is confirmed by measuring substrate only. For sample 1, 2θ peaks located at ~ 19.12°, ~ 38.47°, and ~ 59.19° correspond to $(\bar{2}01)$, $(\bar{4}02)$, and $(\bar{6}03)$ orientations of beta phase ZnGaO, respectively, indicating the growth direction of $<\bar{2}01>$ along $<0001>$ c-sapphire. An additional plane of (113) at ~ 60.36° was also detected. The XRD pattern suggests that sample 1 is pure β-phase Ga_2O_3. For sample 2–7, similar 2θ peak positions located at ~ 18.6°, ~ 37.8°, and ~ 57.6° were observed, although peaks shift towards a lower angle compared to that of sample 1. This can be due to either Zn^{2+} (74 pm) having a larger ionic radius than Ga^{3+} (62 pm), which results in a larger plane distance in beta phase, or the change of crystal structure from beta to spinel phase[59,60].

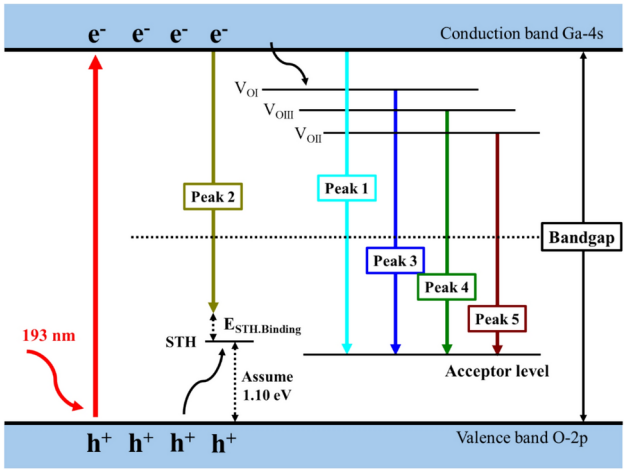

Fig. 4. Schematic band diagram with intermediate energy levels and optical transitions corresponding to the deconvoluted PL peaks of sample 1–9.

Sample	V_{OI} (eV)	V_{OII} (eV)	V_{OIII} (eV)	STH binding energy (eV)	$V_{Ga\text{-}O}$ (eV) [V_{Zn} or V_{Ga}] (V_{Ga} or Zn_{Ga})
1	0.91	1.78	1.26	0.28	0.80
2	0.97	1.83	1.15	N/A	0.82
3	1.20	2.02	1.87	N/A	[0.84]
4	1.14	1.86	1.51	0.33	[0.85]
5	1.11	1.90	1.43	0.60	[0.77]
6	1.17	2.21	1.81	0.69	[0.78]
7	0.85	1.79	1.14	0.24	(0.88)
8	0.82	1.78	1.24	0.18	(0.88)
9	0.93	1.83	1.24	0.15	(0.69)

Table 2. Calculated oxygen vacancy energies below conduction band, STH binding energy, and acceptor level energy above valance band for sample 1–9.

Because beta phase and spinel phase have similar out-of-plane peak positions, in-plane RSM was performed to identify the crystal structure, as shown in Fig. 2. Figure 2a shows in-plane RSM of sample 1, and a strong signal located at $2\theta_\chi \sim 61.35^\circ$ indicates the beta phase structure of (020) plane. Figure 2b shows in-plane RSM of sample 2, and two signals located at $2\theta_\chi \sim 61.5^\circ$ and $\sim 64^\circ$ were observed, indicating a mixture of beta phase (020) plane and spinel phase (440) plane, respectively. Figure 2c–i shows in-plane RSM of sample 3–9, and the signal located at $2\theta_\chi \sim 63^\circ$ indicates the spinel phase structure of (440) plane. Based on the in-plane RSM results, it can be concluded that for sample 3–9, 2θ peaks located at $\sim 18.6^\circ$, $\sim 37.8^\circ$, and $\sim 57.6^\circ$ correspond to (111), (222), and (511) orientation of spinel phase, respectively, indicating the growth direction of $<111>$ along $<0001>$ c-sapphire. Next, according to Bragg's law $2dsin\theta = n\lambda$, where d is the distance between the two planes, θ is the incident beam angle from the scattering plane, n is the diffraction order, and λ is the wavelength of the x-ray, lattice parameters can be extracted from $\theta/2\theta$ scan and in-plane RSM. To calculate lattice parameters for beta structure, $b = 2d$ was used for in-plane RSM, $a = 2 \times \frac{d}{\cos(39.9^\circ)}$ and $c = 1 \times \frac{d}{\cos(36.2^\circ)}$ for $\theta/2\theta$ scan. For spinel structure, $a = \frac{d}{\sqrt{h^2+k^2+l^2}}$ was used for in-plane RSM and assuming $a = b = c$ because of the cubic structure. These calculated lattice parameters are listed in Table 1 and plotted as a function of Zn composition in Fig. S5. These lattice parameters are similar to reported values for beta phase Ga_2O_3[61,62] and spinel phase $ZnGa_2O_4$[63,64], respectively. In spinel samples, the lattice parameter increases slightly from 8.25 to 8.35 Å as the Zn composition increases.

Figure 3a–i show room temperature PL spectra and the peak deconvolution of sample 1–9. The spectra of all samples except sample 2 and 3 are deconvoluted into five peaks. Figure 4 shows a schematic diagram of optical transition energy levels of the five deconvoluted peaks. Peak 1–5 corresponds to UV, violet, blue, green, and red emissions. As seen from Fig. 3a, which is PL spectrum of sample 1 with Zn composition of 0.0 at% (β-Ga_2O_3), UV emission is due to electron–hole recombination from conduction band to gallium-oxygen complex vacancies ($V_{Ga\text{-}O}$). By using the equation $E_{V_{Ga-O}} = E_g - E_{UV}$, where E_{UV} is the energy of the UV emission, and $E_{V_{Ga-O}}$ is the energy of $V_{Ga\text{-}O}$, the estimated location of $V_{Ga\text{-}O}$ is 0.91 eV above the valence band edge. Violet emission is due to recombination from the conduction band to STHs. Similar violet emission

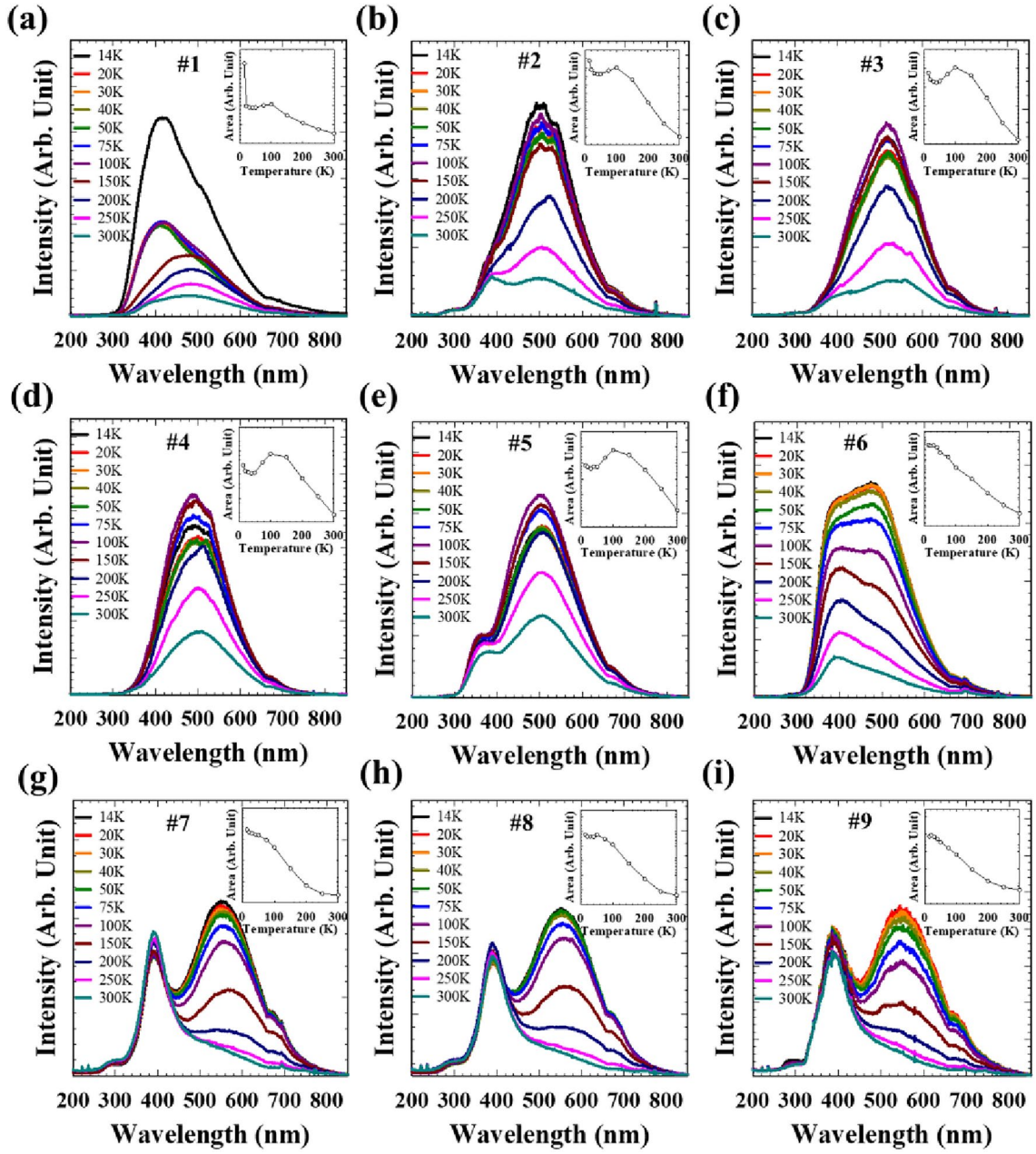

Fig. 5. Temperature-dependent PL spectra under 193 nm excitation with Zn composition of (**a**) 0.0 at%, (**b**) 0.9 at%, (**c**) 3.4 at%, (**d**) 7.3 at%, (**e**) 16.5 at%, (**f**) 33.1 at%, (**g**) 43.9 at%, (**h**) 45.2 at%, (**i**) 48.0 at%. The inserted graph shows the integrated PL peak area as a function of temperature.

energy was observed and reported by others[65,66]. STHs exist in some oxide materials, and here the energy is assumed to be 1.10 eV above the valence band[67]. By using the equation $E_{PL} = E_g - E_{STH} - E_{STH\cdot binding}$, where $E_{STH\cdot binding}$ is the binding energy of STHs, $E_{STH\cdot binding}$ can be calculated to be approximately 0.39 eV[68,69]. Blue, green, and red emissions are due to optical transitions between three oxygen vacancies (V_O) and $V_{Ga\text{-}O}$, commonly known as donor-to-acceptor pair recombination (DAP). Similar emission peaks in the visible light range were observed in literature[65,70,71]. By using the equation $E_{V_O} = E_g - E_{PL} - E_{V_{Ga-O}}$, the three oxygen vacancies V_{OI}, V_{OIII}, and V_{OII} levels are estimated at 0.91 eV, 1.26 eV, and 1.78 eV below the conduction band edge, respectively. In the PL spectrum of sample 2 with Zn composition of 0.9 at% as seen in Fig. 3b, only 4 deconvoluted peaks were observed: UV, blue, green, and red emission. The violet emission, which is the transition between conduction band and STHs, cannot be observed. This could be due to the fact that the mixture phase has a lower-quality film, which results in stronger emission from the transition of DAP and the transition of conduction band to acceptor level. The origin of the blue, green, and red emissions are from transitions between three V_O levels and $V_{Ga\text{-}O}$. By using the equation $E_{V_{Ga-O}} = E_g - E_{UV}$, the $V_{Ga\text{-}O}$ level energy for sample 2 is estimated to be 0.82 eV above the valance band maximum. Similar to sample 2, sample

3 only has 4 deconvoluted peaks as seen in Fig. 3c, which may be due to the weak spinel crystal structure. The acceptor level energy for sample 3 is calculated to be 0.84 eV above the valence band. Figure 3d–f show PL spectra of sample 4–6 with Zn composition of 7.3, 16.5, and 33.1 at%, respectively. The DAP emissions could originate from optical transitions between three V_O and Zn vacancies (V_{Zn}) or Ga vacancies (V_{Ga}) because these spinel samples have lower Zn compositions compared to the normalized cations of spinel $ZnGa_2O_4$. The acceptor level energy for sample 4–6 is estimated to be 0.85, 0.77, and 0.78 eV, respectively. Figure 3g–i show PL spectra of sample 7–9 with Zn composition of 43.9, 45.2, and 48.0 at%, respectively. These samples have higher Zn composition compared to the normalized cations of spinel $ZnGa_2O_4$. The calculated STH binding energy is 0.24, 0.18, and 0.15 eV for sample 7–9, respectively. These are similar to the theoretically estimated value of $E_{STH.binding} = 0.21$eV from Lyons et al.[51] The origin of DAP emissions can be attributed to the transitions between three V_O levels and acceptor level, which could be Zn replaced Ga site (Zn_{Ga}) or V_{Ga}. The acceptor level energy for sample 7–9 is 0.88, 0.88, and 0.69 eV, respectively. All calculated values of oxygen vacancy levels, STH binding energies, and acceptor level energies are listed in Table 2. The energies of the three oxygen vacancies are referenced to the conduction band, and the acceptor levels are referenced to the valence band.

Figure 5 shows temperature-dependent PL spectra with temperatures ranging from 14 K to room temperature, and the inserted graph shows the integrated PL peak area as a function of temperature. As seen from Fig. 5, all samples exhibit general trend of the decrease of PL intensity as the temperature increases in the higher temperature range. This is known as the positive thermal quenching effect, where non-radiative recombination becomes more dominant under high temperature, which results in the decrease of the PL intensity. In the meantime, all samples, especially sample 1–5, show that the PL intensity increases as the temperature increases in a narrower and lower temperature range, which is ascribed to the negative thermal quenching effect. Negative thermal quenching exists because the rates of optical transitions involving intermediate energy levels in the forbidden gap including donor–acceptor pair transitions increase as the temperature increases and these transitions have dominated radiative recombination within the temperature range. To qualitatively describe the temperature-dependent PL intensity, the following equation is used[72,73]: $I(T) = \frac{1+ae^{(-E_{NA}/kT)}}{1+be^{(-E_A/kT)}}$, where $I(T)$ is the integrated PL intensity at temperature T, E_A is the nonradiative recombination activation energy that results in positive thermal quenching process, E_{NA} represents the activation energy of optical transitions from intermediate states that results in negative thermal quenching process, T is the temperature in Kelvin, and a and b are rate parameters. To extract nonradiative recombination activation energies at high temperature, the term $ae^{(-E_{NA}/kT)}$ is much smaller than 1, and the term $be^{(-E_A/kT)}$ is much larger than 1, so the above equation is simplified to $I(T) \propto e^{(E_A/kT)}$[74–76]. Figure S6 shows the Arrhenius plot of sample 1–9. The activation energy of the nonradiative recombination is 13 meV for sample 1 with β-phase structure, 43 meV for sample 2 with mixture phase, and between 11 to 32 meV for sample 3–9 with spinel structure. It is noted that Arrhenius plot cannot be fitted in low-temperature range due to negative thermal quenching effect. Within this temperature range, as seen from the equation mentioned above, the numerator dominates the PL intensity compared with the contribution from the denominator, which results in an increase of the PL intensity in the temperature range.

Conclusion

In this work, 9 ZnGaO samples with Zn composition ranging from 0.0 to 48.0 at% were grown using a plasma-assisted MBE system. When Zn composition is increased to 0.9 at%, the sample exhibits a mixture of beta and spinel structure. When Zn composition is 3.4 at%, the sample exhibits weak spinel structure. When Zn composition is larger than 7.3 at%, all samples exhibit spinel structure. PL studies of these samples using a 193 nm laser as excitation were carried out to systematically analyze and understand the optical transition of these samples. The STH binding energy and the position of the three oxygen vacancies and acceptor levels were revealed. This study paves a way towards the application of spinel $ZnGa_2O_4$ for deep ultraviolet photodetectors and other optoelectronic applications.

Methods

Film growth

A 2-inch c-plane sapphire wafer was used as substrate in this work and was cleaned by using piranha solution (H_2SO_4: H_2O_2 = 5:3) to remove any organic contamination, then rinsed with DI water to remove residual acid from the substrate. After being blow-dried by nitrogen, c-plane sapphire substrate was introduced into the loadlock of an SVT Associates plasma-assisted molecular beam epitaxy (MBE) chamber. 6N Ga and 6N Zn from Alfa Aesar were used for sample growth. The composition ratio of Zn and Ga can be adjusted by tuning the effusion cell temperature of Zn and Ga. Oxygen flow rate was set to 2.5 sccm and the RF power was 400 W. Pre-growth annealing of substrate at 800 °C for 15 min was performed, then substrate temperature was decreased to 450 °C for sample growth. After that, substrate temperature was increased to 700 °C and a post-growth annealing process with oxygen was carried out for 20 min.

Film characterization

The thickness of samples was measured using a Nikon Profilm3D profilometer. The surface morphology of ZnGaO thin films were measured using a TESCAN Vega3 SBH Scanning Electron Microscopy (SEM) system at a voltage of 10 kV, a beam intensity of 7, and a working distance of ~ 7.5 mm. The Zn/Ga atomic ratio was measured using a Quantax energy dispersive x-ray (EDX) system at a voltage of 15 kV, a beam intensity of 15, and a working distance of 14 mm. To analyze the ratio of Zn, Ga, and O composition and valence band spectra for each sample, X-ray photoelectron spectroscopy (XPS) characterizations of different ZnGaO thin films were carried out by a Kratos AXIS ULTRADLD XPS system using an Al Kα X-ray source. During measurement,

vacuum pressure was kept below 3×10^{-9} torr. X-Ray diffraction (XRD) in θ/2θ scan mode was measured using a PANalytical Empyrean Series 2 XRD system with Cu Kα x-ray (λ = 0.15405 nm) to understand the out-of-plane crystal orientation. The in-plane distance and crystal structure were evaluated using a Rigaku SmartLab X-ray Diffractometer with Cu x-ray tube (λ = 0.1540 nm) and operational voltage and current of 40 kV and 44 mA, respectively. Absorbance and transmittance spectra of ZnGaO samples were obtained using an Agilent Cary 5000 Double Beam UV/VIS/NIR spectrometer from 200 to 800 nm with a resolution of 0.1 nm. PL spectra were obtained using a COHERENT ExciStar 193 nm laser system equipped with ArF gas source.

Data availability

All data generated or analyzed during this study are included in this published article and in Supplementary Information files.

Received: 27 February 2025; Accepted: 25 April 2025
Published online: 14 May 2025

References

1. Higashiwaki, M. β-gallium oxide devices: Progress and outlook. *Physica Status Solidi (RRL)—Rapid Res. Lett.* **15**, 2100357 (2021).
2. Qin, Y. et al. Review of deep ultraviolet photodetector based on gallium oxide. *Chin. Phys. B* **28**, 018501 (2019).
3. Zhang, J. et al. Deep UV transparent conductive oxide thin films realized through degenerately doped wide-bandgap gallium oxide. *Cell Rep. Phys. Sci.* **3**(3), 100801. https://doi.org/10.1016/j.xcrp.2022.100801 (2022).
4. Kaur, D. & Kumar, M. A strategic review on gallium oxide based deep-ultraviolet photodetectors: Recent progress and future prospects. *Adv. Opt. Mater.* **9**, 2002160 (2021).
5. Tadjer, M. J. Toward gallium oxide power electronics. *Science* **378**, 724–725 (2022).
6. Kaur, D., Ghosh, A. & Kumar, M. A strategic review on gallium oxide based power electronics: Recent progress and future prospects. *Mater. Today Commun.* **33**, 104244 (2022).
7. Stepanov, S., Nikolaev, V., Bougrov, V. & Romanov, A. Gallium OXIDE: Properties and applica 498 a review. *Rev. Adv. Mater. Sci.* **44**, 63–86 (2016).
8. Chen, Y. et al. Bandgap engineering of Gallium oxides by crystalline disorder. *Mater. Today Phys.* **18**, 100369 (2021).
9. Oh, S., Kim, J., Ren, F., Pearton, S. J. & Kim, J. Quasi-two-dimensional β-gallium oxide solar-blind photodetectors with ultrahigh responsivity. *J. Mater. Chem. C* **4**, 9245–9250 (2016).
10. Hao, Y. Gallium oxide: Promise to provide more efficient life. *J. Semicond.* **40**, 010301 (2019).
11. Tak, B. R. et al. Recent advances in the growth of gallium oxide thin films employing various growth techniques—a review. *J. Phys. D Appl. Phys.* **54**, 453002 (2021).
12. Zhou, H. et al. A review of the most recent progresses of state-of-art gallium oxide power devices. *J. Semicond.* **40**, 011803 (2019).
13. Razeghi, M. et al. A review of the growth, doping, and applications of Beta-Ga_2O_3 thin films. *Oxide-based Mater. Dev. IX* **10533**, 21–44 (2018).
14. Yuan, Y. et al. Toward emerging gallium oxide semiconductors: A roadmap. *Fund. Res.* **1**, 697–716 (2021).
15. Yang, T. et al. Metal–semiconductor–metal photodetectors based on β-MgGaO thin films. *ACS Appl. Electron. Mater.* **5**, 2122–2130 (2023).
16. Yang, T. et al. Investigation of phase transition and ultrawide band gap engineering in MgGaO semiconductor thin films. *ACS Appl. Opt. Mater.* **1**, 1670–1678 (2023).
17. Chen, Y.-C. et al. Bandgap tunable ZnGaO thin films grown by atomic layer deposition for high-performance ultraviolet photodetection. *ACS Mater. Lett.* **5**, 2852–2861 (2023).
18. Guo, D. et al. Decrease of oxygen vacancy by Zn-doped for improving solar-blind photoelectric performance in β-Ga_2O_3 thin films. *Electron. Mater. Lett.* **13**, 483–488 (2017).
19. Zhao, X. et al. Improvement for the performance of solar-blind photodetector based on β-Ga_2O_3 thin films by doping Zn. *J. Phys. D Appl. Phys.* **50**, 085102 (2017).
20. Chikoidze, E. et al. p-type ultrawide-band-gap spinel $ZnGa_2O_4$: New perspectives for energy electronics. *Cryst. Growth Des.* **20**, 2535–2546 (2020).
21. Tao, J. et al. Investigation of growth characteristics, compositions, and properties of atomic layer deposited amorphous Zn-doped Ga_2O_3 films. *Appl. Surf. Sci.* **476**, 733–740 (2019).
22. Alema, F. et al. Solar blind photodetector based on epitaxial zinc doped Ga_2O_3 thin film. *Phys. Status Solidi (A)* **214**(5), 1600688. https://doi.org/10.1002/pssa.201600688 (2017).
23. Hsu, C.-H. et al. Improved performance of solar blind ultraviolet photodetectors by spatial ALD Zn-doped Ga_2O_3 film and post-annealing. *Surf. Coat. Technol.* **497**, 131798. https://doi.org/10.1016/j.surfcoat.2025.131798 (2025).
24. Choi, Y., Lee, S.-S., Lee, W.-J. & Park, I.-K. Zn-doping induced phase control mechanism of Ga_2O_3 thin films by spray pyrolysis deposition for application of solar-blind ultraviolet photodetector. *Mater. Today Chem.* **33**, 101738 (2023).
25. Han, D. et al. Self-powered solar-blind $ZnGa_2O_4$ UV photodetector with ultra-fast response speed. *Sens. Actuators A* **315**, 112354 (2020).
26. Jang, Y. et al. Thin film transistors based on ultra-wide bandgap spinel $ZnGa_2O_s$. *Appl. Phys. Lett.* https://doi.org/10.1063/5.0007716 (2020).
27. Horng, R.-H., Huang, C.-Y., Ou, S.-L., Juang, T.-K. & Liu, P.-L. Epitaxial growth of $ZnGa_2O_4$: A new, deep ultraviolet semiconductor candidate. *Cryst. Growth Des.* **17**, 6071–6078 (2017).
28. Chikoidze, E. et al. P-type ultrawide-band-gap spinel $ZnGa_2O_4$. (2020).
29. Guo, A. et al. Pulsed laser deposition of $ZnGa_2O_4$ thin films on Al_2O_3 and Si substrates for deep optoelectronic devices applications. *Appl. Phys. Express* **16**, 021004 (2023).
30. Safeera, T. et al. Zinc gallate and its starting materials in solid state reaction route-A comparative study. *Mater. Chem. Phys.* **181**, 21–25 (2016).
31. Soundar, R. et al. Deep blue emission and latent finger print detection analysis of zinc gallate nanoparticles. *Mater. Res. Bull.* **174**, 112701 (2024).
32. Zubkins, M. et al. Deposition and photoluminescence of zinc gallium oxide thin films with varied stoichiometry made by reactive magnetron co-sputtering. *J. Alloy. Compd.* **976**, 173218 (2024).
33. Li, D., Wang, Y., Xu, K., Li, L. & Hu, Z. Persistently luminescent and photocatalytic properties of $ZnGa_2O_4$ phosphors. *Mater. Res. Express* **2**, 046202 (2015).
34. Park, K.-W., Yun, Y.-H. & Choi, S.-C. Photoluminescence characteristics of $ZnGa_2O_4$ thin films prepared by chemical solution method. *Solid State Ion.* **177**, 1875–1878 (2006).
35. Bae, J. S. et al. Photoluminescence behaviors in $ZnGa_2O_4$ thin film phosphors deposited by a pulsed laser ablation. *Thin Solid Films* **424**, 291–295 (2003).

36. Jin, M. et al. A new persistent luminescence phosphor of $ZnGa_2O_4$: Ni^{2+} for the second near-infrared transparency window. *J. Alloy. Compd.* **931**, 167491 (2023).
37. Yi, Z., Liu, P. & Xu, Y. Multimode dynamic photoluminescence of Bi^{3+}-activated $ZnGa_2O_4$ for optical information encryption. *Inorg. Chem.* **62**, 9671–9678 (2023).
38. Gerus, A., Boiko, V., Ciaramitaro, V. C., Saladino, M. L. & Hreniak, D. Controlling a defect structure of the $ZnGa_2O_4$: Cr^{3+} spinel through synthesis parameters for persistent luminescence optimization. *Mater. Res. Bull.* **168**, 112473 (2023).
39. Gupta, S. K., Sudarshan, K., Chandrashekhar, D., Balhara, A. & Mohapatra, M. Solid solution of Cr^{3+} doped $ZnGa_2O_4$ and Zn_2SnO_4 to create cation inversion and its role on persistent deep red emission. *J. Lumin.* **257**, 119697 (2023).
40. Nunes, M. et al. Nanosized $ZnGa_2O_4$:Cr^{3+} Spinels as Highly Luminescent Materials for Bioimaging. *ACS Appl. Nano Mater.* **2**(11), 6918–6927. https://doi.org/10.1021/acsanm.9b01417 (2019).
41. Tran, T. et al. Photoluminescence properties of $ZnGa_2O_4$: Mn powder phosphors. *J. Appl. Phys.* **78**, 5691–5695 (1995).
42. Liu, J., Duan, X., Zhang, Y. & Jiang, H. Cation distribution and photoluminescence properties of Mn-doped $ZnGa_2O_4$ nanoparticles. *J. Phys. Chem. Solids* **81**, 15–19 (2015).
43. Yu, C. F. & Lin, P. Manganese-activated luminescence in $ZnGa_2O_4$. *J. Appl. Phys.* **79**, 7191–7197 (1996).
44. Shea, L., Datta, R. & Brown, J. Photoluminescence of Mn^{2+}-activated $ZnGa_2O_4$. *J. Electrochem. Soc.* **141**, 1950 (1994).
45. Hsu, K.-H., Yang, M.-R. & Chen, K.-S. A study of $ZnGa_2O_4$ phosphor prepared by the solid method. *J. Mater. Sci. Mater. Electron.* **9**, 283–288 (1998).
46. Kim, K., Kim, K., Kwon, H.-G., Kim, S. & Kim, S.-W. Lanthanide-doped zinc gallium oxide ($ZnGa_2O_4$) nanocrystals and their engineered photoluminescence. *Macromol. Res.* **33**(1), 69–75. https://doi.org/10.1007/s13233-024-00312-3 (2024).
47. Shi, Q., Zhang, J., Cai, C., Cong, L. & Wang, T. Synthesis and photoluminescent properties of Eu^{3+}-doped $ZnGa_2O_4$ nanophosphors. *Mater. Sci. Eng. B* **149**, 82–86 (2008).
48. Kamal, C. S. et al. Influence of Ge4+ doping on photo-and electroluminescence properties of $ZnGa_2O_4$. *J. Alloy. Compd.* **852**, 156967 (2021).
49. Kananen, B. E. et al. Self-trapped holes in β-Ga_2O_3 crystals. *J. Appl. Phys.* https://doi.org/10.1063/1.5007095 (2017).
50. Gake, T., Kumagai, Y. & Oba, F. First-principles study of self-trapped holes and acceptor impurities in Ga_2O_3 polymorphs. *Phys. Rev. Mater.* **3**, 044603 (2019).
51. Lyons, J. L. Self-trapped holes and polaronic acceptors in ultrawide-bandgap oxides. *J. Appl. Phys.* https://doi.org/10.1063/5.0077030 (2022).
52. Tsai, M.-Y., Bierwagen, O., White, M. E. & Speck, J. S. β-Ga_2O_3 growth by plasma-assisted molecular beam epitaxy. *J. Vac. Sci. Technol., A* **28**, 354–359 (2010).
53. Ahmadi, E. et al. Ge doping of β-Ga_2O_3 films grown by plasma-assisted molecular beam epitaxy. *Appl. Phys. Express* **10**, 041102 (2017).
54. Oshima, T., Arai, N., Suzuki, N., Ohira, S. & Fujita, S. Surface morphology of homoepitaxial β-Ga_2O_3 thin films grown by molecular beam epitaxy. *Thin Solid Films* **516**, 5768–5771 (2008).
55. Oshima, T., Okuno, T. & Fujita, S. Ga_2O_3 thin film growth on c-plane sapphire substrates by molecular beam epitaxy for deep-ultraviolet photodetectors. *Jpn. J. Appl. Phys.* **46**, 7217 (2007).
56. Look, D. C. et al. Characterization of homoepitaxial p-type ZnO grown by molecular beam epitaxy. *Appl. Phys. Lett.* **81**, 1830–1832 (2002).
57. Chen, Y. et al. Plasma assisted molecular beam epitaxy of ZnO on c-plane sapphire: Growth and characterization. *J. Appl. Phys.* **84**, 3912–3918 (1998).
58. Xiu, F. X. et al. High-mobility Sb-doped p-type ZnO by molecular-beam epitaxy. *Appl. Phys. Lett.* https://doi.org/10.1063/1.2089183 (2005).
59. Miyaji, F., Kono, Y. & Suyama, Y. Formation and structure of zinc-substituted calcium hydroxyapatite. *Mater. Res. Bull.* **40**, 209–220 (2005).
60. Nikolova, V., Angelova, S., Markova, N. & Dudev, T. Gallium as a therapeutic agent: A thermodynamic evaluation of the competition between Ga^{3+} and Fe^{3+} ions in metalloproteins. *J. Phys. Chem. B* **120**, 2241–2248 (2016).
61. Geller, S. Crystal structure of β-Ga_2O_3. *J. Chem. Phys.* **33**, 676–684 (1960).
62. Yamaguchi, K. First principles study on electronic structure of β-Ga_2O_3. *Solid State Commun.* **131**, 739–744 (2004).
63. Errandonea, D., Kumar, R. S., Manjón, F. J., Ursaki, V. V. & Rusu, E. V. Post-spinel transformations and equation of state in $ZnGa_2O_4$: Determination at high pressure by in situ x-ray diffraction. *Phys. Rev. B* **79**(2), 024103. https://doi.org/10.1103/PhysRevB.79.024103 (2009).
64. Rafiezadeh, S. et al. Enhanced luminescence and photocatalytic activity in highly inverted spinel $ZnGa_2O_4$ nanoplates. *ACS Appl. Nano Mater.* **8**(2), 1033–1041. https://doi.org/10.1021/acsanm.4c05782 (2025).
65. Thapa, D., Lapp, J., Lukman, I. & Bergman, L. Ultra-wide bandgap β-Ga_2O_3 films: Optical, phonon, and temperature response properties. *AIP Adv.* **11**, (2021).
66. Onuma, T. et al. Modeling and interpretation of UV and blue luminescence intensity in β-Ga_2O_3 by silicon and nitrogen doping. *J. Appl. Phys.* https://doi.org/10.1063/1.5030612 (2018).
67. Wang, Y. et al. Incident wavelength and polarization dependence of spectral shifts in β-Ga_2O_3 UV photoluminescence. *Sci. Rep.* **8**, 18075 (2018).
68. Yang, T. et al. Photoluminescence study of $MgGa_2O_4$ spinel oxide films grown by molecular beam epitaxy. *Appl. Phys. Lett.* https://doi.org/10.1063/5.0218242 (2024).
69. Varley, J. B., Janotti, A., Franchini, C. & Van de Walle, C. G. Role of self-trapping in luminescence and p-type conductivity of wide-band-gap oxides. *Phys. Rev. B* **85**(8), 081109. https://doi.org/10.1103/PhysRevB.85.081109 (2012).
70. Ho, Q. D., Frauenheim, T. & Deák, P. Origin of photoluminescence in β-Ga_2O_3. *Phys. Rev. B* **97**, 115163 (2018).
71. Huh, Y.-Y., Jo, C.-H., Ichimura, M. & Koh, J.-H. Low-temperature deposition of β-Ga_2O_3 thin films employing in situ pulsed laser-assisted RF sputtering system. *Mater. Sci. Semicond. Process.* **179**, 108428 (2024).
72. Junling, W., Rui, W., Tiancheng, Y., Yong, Z. & Rong, W. Negative thermal quenching of the defects in GaInP top cell with temperature-dependent photoluminescence analysis. *Nucl. Instrum. Methods Phys. Res. Sect. B* **414**, 1–3 (2018).
73. Shibata, H. Negative thermal quenching curves in photoluminescence of solids. *Jpn. J. Appl. Phys.* **37**, 550 (1998).
74. Krustok, J., Collan, H. & Hjelt, K. Does the low-temperature Arrhenius plot of the photoluminescence intensity in CdTe point towards an erroneous activation energy? *J. Appl. Phys.* **81**, 1442–1445 (1997).
75. Ikhmayies, S. J. & Ahmad-Bitar, R. N. Temperature dependence of the photoluminescence spectra of CdS: In thin films prepared by the spray pyrolysis technique. *J. Lumin.* **142**, 40–47 (2013).
76. Fang, Y. et al. Investigation of temperature-dependent photoluminescence in multi-quantum wells. *Sci. Rep.* **5**, 12718 (2015).

Author contributions

C.S. led the investigation and data curation, did data analysis, and wrote the main manuscript text. T.Y. supported the data analysis. K.R. supported the data curation and data analysis. J.L. formed the conceptualization, supported the investigation, supervised the project, and revised the manuscript. All authors reviewed the manuscript.

Funding
This work was supported by the National Science Foundation (ECCS-2105566) and the Air Force Office of Scientific Research under DURIP award number FA9550-22-1-0505. The authors acknowledge the use of the XPS instrument at UC Riverside, which is supported by the National Science Foundation (DMR-0958796).

Declarations

Competing interests
The authors declare no competing interests.

Additional information
Supplementary Information The online version contains supplementary material available at https://doi.org/10.1038/s41598-025-00234-9.

Correspondence and requests for materials should be addressed to J.L.

Reprints and permissions information is available at www.nature.com/reprints.

Publisher's note Springer Nature remains neutral with regard to jurisdictional claims in published maps and institutional affiliations.